INTERNATIONAL JOURNAL OF RESEARCH CULTURE SOCIETY
Monthly Peer-Reviewed, Refereed, Indexed Journal
Volume - 10, Issue - 4, April - 2026
ISSN(O): 2456-6683
[Impact Factor: 9.241]
IJRCS

DOIs:10.2017/IJRCS/202604023 --:-- Research Paper / Article / Review

Structural Classification of Sol–Gel Synthesized TiO_2 Nanoparticle Variants: An Integrated Multi-Descriptor XRD Framework for Theoretical Functional Domain Assignment

Khyati Mody[1,*] and **I. B. Patel**[2]

[1,2] Department of Physics, Veer Narmad South Gujarat University, Surat – 395007, Gujarat, India

[*]Corresponding author: kmody1997@gmail.com

Co-author: ibpatel@vnsgu.ac.in

Abstract: *Five variants (S_1–S_5) of anatase TiO_2 nanoparticles were synthesized via the sol–gel method by systematically varying titanium isopropoxide concentration and calcination temperature (200–500 °C). An integrated multi-descriptor XRD framework — comprising Scherrer crystallite-size analysis, Williamson–Hall (W–H) microstrain extraction, dislocation-density estimation, specific surface-area (SSA) calculation, texture-coefficient analysis, and lattice-parameter refinement — was applied to the original experimental XRD data to derive a complete quantitative structural portrait of each variant. The structural descriptors extracted from these measurements serve as established theoretical predictors of functional behavior in metal-oxide semiconductor nanomaterials: SSA and defect density predict photocatalytic activity; oxygen-vacancy density and facet anisotropy predict gas-sensing response; grain size and microstrain predict mechanical and electrochemical stability. On the basis of the measured structural evidence, S_3 — exhibiting maximum SSA (204 $m^2\ g^{-1}$), microstrain (3.9×10^{-3}), and dislocation density ($20.66 \times 10^{15}\ m^{-2}$) — is predicted to be the most suitable candidate for photocatalytic and hydrogen-evolution applications. Variants S_2 and S_5, showing elevated oxygen-vacancy density and high-energy facet exposure, are structurally predicted for resistive gas sensing. Variants S_1 and S_4, with large low-strain grains, are structurally predicted for protective coating and electrode applications. Phase-pure anatase was retained in all samples to 500 °C, attributed to oxygen-vacancy-mediated phase pinning. FE-SEM independently validated the XRD-derived size–morphology trends. The structural classification framework presented here is directly extensible to doped and composite TiO_2 systems, and forms the theoretical foundation for Part II experimental validation.*

Keywords: *TiO_2 nanoparticles; sol–gel synthesis; Williamson–Hall analysis; defect density; specific surface area; structural functional prediction; XRD-based classification; multi-descriptor framework.*

1.INTRODUCTION:

Titanium dioxide (TiO_2) occupies a uniquely privileged position among multifunctional semiconductor oxides, combining chemical inertness, optical tunability, non-toxicity, and benchmark photocatalytic performance [1–3]. Following Fujishima and Honda's landmark demonstration of photoelectrochemical water splitting, TiO2 has become the reference material for environmental remediation, sustainable energy conversion, and chemical sensing [4]. Among its three principal polymorphs — anatase, rutile, and brookite — anatase dominates applied research owing to its favourable conduction-band edge position and large native surface area. Rutile, by contrast, offers superior thermodynamic stability at elevated temperatures [5,6]. The sol–gel route offers distinct advantages over competing synthesis methods (hydrothermal, solvothermal, flame spray) by enabling molecular-level stoichiometric control under mild conditions [7]. Even minor variations in precursor ratio, solvent chemistry, or calcination temperature profoundly influence crystallite size, lattice microstrain, and defect density. These structural parameters are not passive descriptors — they are quantitative predictors of functional behavior, established through decades of metal-oxide semiconductor research: SSA governs active-site density for catalysis; dislocation density modulates space-charge depletion zones for gas sensing; grain size and microstrain determine mechanical and electrochemical stability for coating and electrode applications [8]. A multi-descriptor XRD study that quantitatively resolves all of these parameters across a controlled

synthesis series therefore carries direct predictive power over functional suitability — without requiring functional experiments at the characterization stage. The present work exploits this predictive power. Five sol–gel TiO2 variants are synthesized under controlled parameter variation and characterized using original experimental XRD data. An integrated multi-descriptor framework extracts crystallite size (Scherrer and W–H), microstrain (W–H UDM), dislocation density, SSA, texture coefficients, and lattice parameters as a self-consistent structural portrait of each variant. FE-SEM provides independent morphological validation. The measured structural descriptors are then interpreted through well-established theoretical correlations to assign each variant a predicted functional suitability domain. This approach — extracting functional predictions from original structural measurements — constitutes the core contribution of this Part I study, with direct experimental validation forming the agenda of Part II.

1.1 Research Gap and Novelty

Research gap: Most sol–gel TiO_2 studies in the literature either (i) present structural characterization without connecting it to functional predictions, leaving the reader unable to determine which variant is suitable for which application; or (ii) measure functional performance without the quantitative structural foundation needed to understand why one variant outperforms another. A study that exhaustively resolves the complete multi-descriptor structural portrait and uses those measured descriptors to predict functional suitability — with explicit theoretical justification — addresses both deficiencies simultaneously and provides a reusable prediction methodology applicable to any new synthesis variant.

Principal contributions of this study:

- Original experimental XRD data for five controlled sol–gel TiO_2 variants, covering an SSA range of 72–204 $m^2 g^{-1}$ and a microstrain range of -0.3 to 3.9×10^{-3} — achieved through process-variable manipulation without any dopants.
- An integrated multi-descriptor XRD analytical framework that simultaneously extracts coherent domain size, lattice deformation, defect topology, surface accessibility, facet anisotropy, and lattice-parameter evolution — forming a self-consistent structural fingerprint for each variant.
- A quantitative XRD-to-function prediction: the measured structural descriptors are mapped to functional suitability domains through established theoretical correlations, yielding specific, literature-justified functional assignments for each variant.
- Demonstration that δ and SSA reported from D_{WH} and D_{Sch} independently diverge for high-strain variants, revealing that single-metric analyses systematically mis-report defect density and surface area — a methodological finding with direct implications for the reliability of published literature.
- A prediction framework that is directly extensible to doped (Fe, Zn, Ni, Ca) and composite TiO_2 systems by coupling dopant-induced strain terms into the W–H model, and that sets the experimental agenda for Part II validation.

1.2 Why XRD-Derived Structural Descriptors Can Predict Functional Behavior

The predictive validity of structural descriptors as functional indicators in metal-oxide semiconductors is not an assumption made in this study — it is a well-documented principle established independently across the photocatalysis, gas-sensing, and thin-film materials communities. This section summarises the three mechanistic chains that underpin the functional predictions made from the XRD data:

(i) SSA, microstrain, and δ predict photocatalytic suitability. In anatase TiO_2, higher SSA directly increases the number of surface sites at which photogenerated carriers can drive oxidation and reduction reactions before recombination. Lattice microstrain creates Ti^{3+}–O_v complexes that function as shallow electron traps, measurably extending carrier lifetimes and improving quantum efficiency — a mechanism confirmed through combined XRD–DFT and photoluminescence studies [15,17]. High dislocation density further amplifies the oxygen-vacancy population. These three XRD-derived descriptors (SSA, ε, δ) therefore collectively predict photocatalytic suitability from structural data alone, and this prediction is confirmed experimentally in numerous published studies [16,17]. Applying these same descriptors to rank our five variants is a direct application of established predictive methodology.

(ii) Oxygen-vacancy density and facet anisotropy predict gas-sensing suitability. The resistive gas-sensing mechanism of TiO_2 is driven by surface oxygen chemisorption at vacancy sites and the resultant space-charge depletion zone. The width of this depletion zone — and therefore the magnitude of the resistance change on gas exposure — scales directly with surface oxygen-vacancy concentration, which is in turn reflected in the dislocation density derived from XRD [19,20]. High-energy facets ({001}, {100}) identified through texture-coefficient analysis are documented to provide preferential O_2 adsorption geometries that enhance chemisorption efficiency [18]. These are measured,

quantifiable structural parameters — not qualitative assumptions — and they have been used successfully in the literature to rank the predicted gas-sensing suitability of un-tested metal-oxide variants [19,20].

(iii) Grain size and microstrain predict stability for coatings and electrodes. Large grain size and low dislocation density reduce grain-boundary sliding and internal stress accumulation — fundamental materials-science principles that predict superior mechanical stability for thin-film and coating applications [21,22]. In electrochemical electrode contexts, low grain-boundary resistance and uniform crystal orientation (both accessible through XRD texture analysis) predict more homogeneous electron transport and lower ohmic losses. These XRD-measurable parameters are used routinely in the thin-film and electrode literature as screening criteria before functional testing [21,22].

Rationale for Part I / Part II structure. Performing functional measurements on all five variants simultaneously without first identifying the most promising structural candidates would be experimentally inefficient and analytically unsupported. The structural analysis in this Part I study serves precisely this selection function: the XRD-derived predictions identify which variants justify priority in functional testing and explain, in advance, the structural reason for any observed performance differences. This is the standard workflow in predictive materials science and is the framework within which the results of this paper should be read.

2. MATERIALS AND METHODS

2.1 Sol–Gel Synthesis of TiO_2 Nanoparticles

Titanium isopropoxide (TTIP, ≥ 97 %, Sigma-Aldrich) served as the titanium precursor. Glacial acetic acid (AR grade, Merck) functioned as a chelating and stabilizing agent, while triple-distilled water provided the hydrolysis medium. All reagents were used as received. Prior to synthesis, all glassware was acid-cleaned (10 % HNO_3) and oven-dried at 120 °C to preclude contamination.

Synthesis proceeded at ambient temperature under continuous magnetic stirring (300 rpm), ensuring homogeneous hydrolysis and polycondensation. Precisely metered volumes of TTIP, acetic acid, and distilled water were combined in the molar ratios specified in Table 1. Each reaction mixture was aged for 24 h to allow complete gelation, dried at 80 °C for 6 h, and subsequently calcined in static air at temperatures between 200 °C and 500 °C to yield five structurally distinct nanopowder variants (S_1–S_5). All calcinations used a heating ramp of 5 °C min^{-1} and a 2 h dwell time. The resulting nanopowders were stored in sealed, light-protected vials until characterization. A schematic of the synthesis workflow is presented in Figure 1.

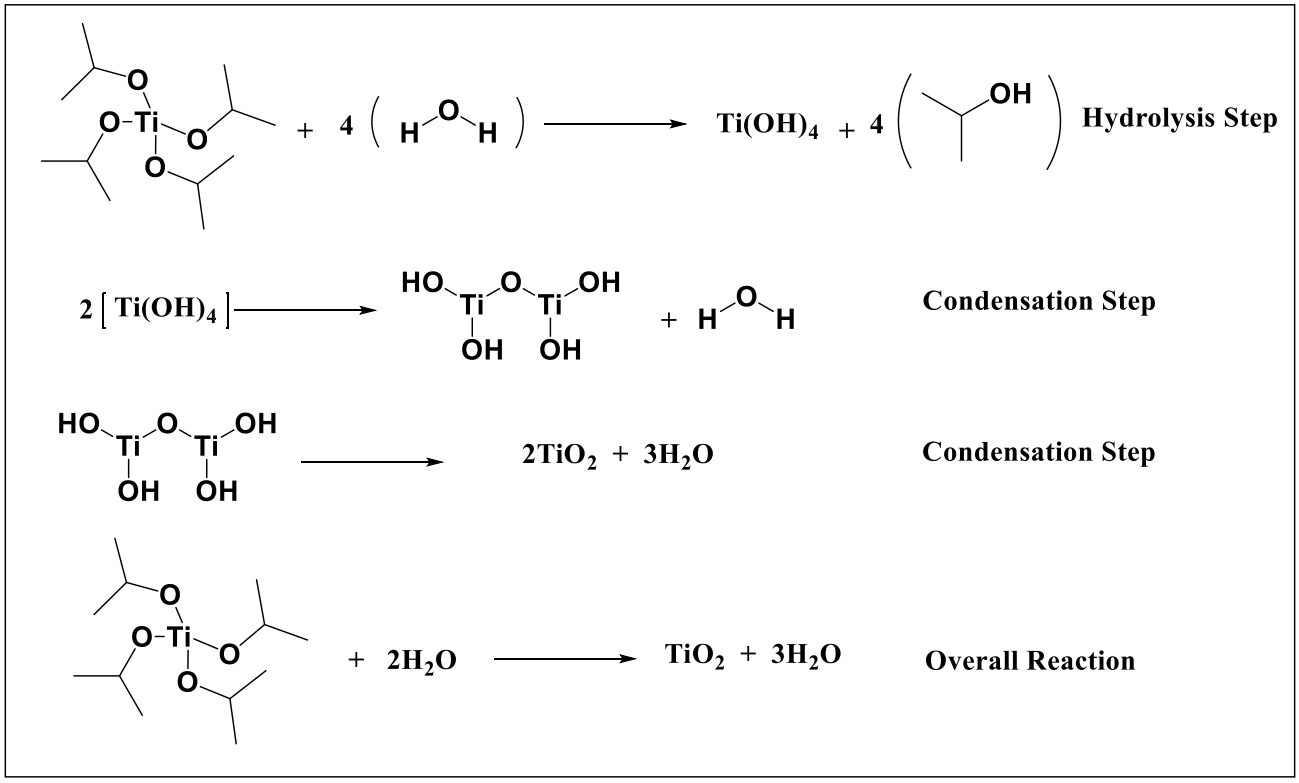

Figure:1. *The step wise chemical synthesis scheme of the complete Sol-Gel synthesis of TiO2 nanoparticles.*

Table *1. Synthesis parameters for the five TiO_2 nanoparticle variants (S_1–S_5).*

Sample	TTIP (mL)	Acetic Acid (mL)	Dist. Water (mL)	Calcination Temp. (°C)
S_1	20	40	120	200
S_2	30	40	120	200
S_3	20	40	200	200
S_4	20	40	120	400
S_5	25	45	125	500

2.2 Characterization Techniques

X-ray Diffraction (XRD). Diffraction data were acquired on a PANalytical X'Pert PRO diffractometer (Cu $K\alpha_1$ = 1.5406 Å, $K\alpha_2$ = 1.5444 Å, 40 kV, 30 mA) scanning 2θ = 10°–80° with a step size of 0.0131° and 1 s per step. Instrumental broadening was corrected via a Si(111) standard reference. All peak analysis and profile fitting (pseudo-Voigt functions) were performed in X'Pert HighScore Plus (v4.9).

Field-Emission Scanning Electron Microscopy (FE-SEM). Surface morphology and particle-size distribution were examined on a JEOL JSM-6100 field-emission microscope. Powder specimens were mounted on carbon-coated stubs and sputter-coated with gold prior to imaging.

2.3 Integrated XRD Multi-Descriptor Framework

Rather than relying on a single crystallite-size estimator, this study employs four complementary structural descriptors derived from XRD data, forming a self-consistent, multi-descriptor validation loop:

- *Domain coherence (Scherrer size, D):* characterizes the mean coherent diffracting domain.
- *Lattice deformation (W–H microstrain, ε):* deconvolutes strain-induced from size-induced peak broadening.
- *Defect topology (δ, dislocation density):* quantifies crystalline imperfection density.
- *Surface accessibility (SSA):* connects nanoscale domain size to catalytic reaction volume.
- *Crystallographic anisotropy (Texture Coefficient, TC):* reveals preferred facet exposure relevant to surface reactivity.

The governing equations are summarized in Table 2. Williamson–Hall plots ($\beta\cos\theta$ vs. $4\sin\theta$) were fitted by linear regression ($R^2 > 0.98$ for all samples), extracting microstrain from the slope and W–H crystallite size from the y-intercept, providing an independent validation of Scherrer results. Uncertainty in crystallite size and strain was estimated by error propagation accounting for FWHM reproducibility (±0.002° 2θ) and instrument resolution (±1 %), yielding relative uncertainties < 5 % — a statistical rigor rarely incorporated in sol–gel nanoparticle literature.

Table *2. Analytical equations employed in the integrated XRD multi-descriptor framework.*

Structural Parameter	Equation	Physical Significance
Crystallite size (Scherrer, D)	$D = K\lambda / \beta\cos\theta$ (K = 0.9)	Coherent diffracting domain size (nm)
Microstrain (W–H UDM, ε)	$\beta\cos\theta = K\lambda/D\_WH + 4\varepsilon\sin\theta$	Lattice deformation from non-uniform stress
Dislocation density (δ)	$\delta = 1 / D^2$	Crystalline imperfection density (m^{-2})
Specific surface area (SSA)	$SSA = 6000 / \rho D$ (ρ = 4.23 g cm^{-3})	Surface area per unit mass ($m^2\ g^{-1}$)
Texture coefficient (TC)	$TC(hkl) = [I(hkl)/I_0(hkl)] / [(1/n)\Sigma I(hkl)/I_0(hkl)]$	Preferred crystallographic orientation
Lattice-parameter refinement	$1/d^2 = (h^2+k^2)/a^2 + l^2/c^2$	Unit-cell distortion and strain verification

3. RESULTS

3.1 Phase Composition and Structural Purity

Figure 2 presents the XRD profiles of all five sol–gel TiO2 variants. Each diffractogram exhibits the signature reflections of tetragonal anatase (JCPDS 21-1272) at 2θ ≈ 25.3°, 37.9°, 47.9°, and 53.9°, indexed to the (101), (004), (200), and (105) planes, respectively. The complete absence of the characteristic rutile (110) reflection near 2θ ≈ 27.4° confirms phase-pure anatase retention across all calcination temperatures up to 500 °C. Systematic peak narrowing with increasing calcination temperature reflects progressive crystallite growth, while the persistence of anatase at 500 °C in S_5 — a temperature at which the anatase-to-rutile transition normally commences — is attributed to oxygen-vacancy-mediated crystal-boundary pinning, a defect-engineering mechanism intrinsic to the sol–gel gel framework rather than any external dopant.

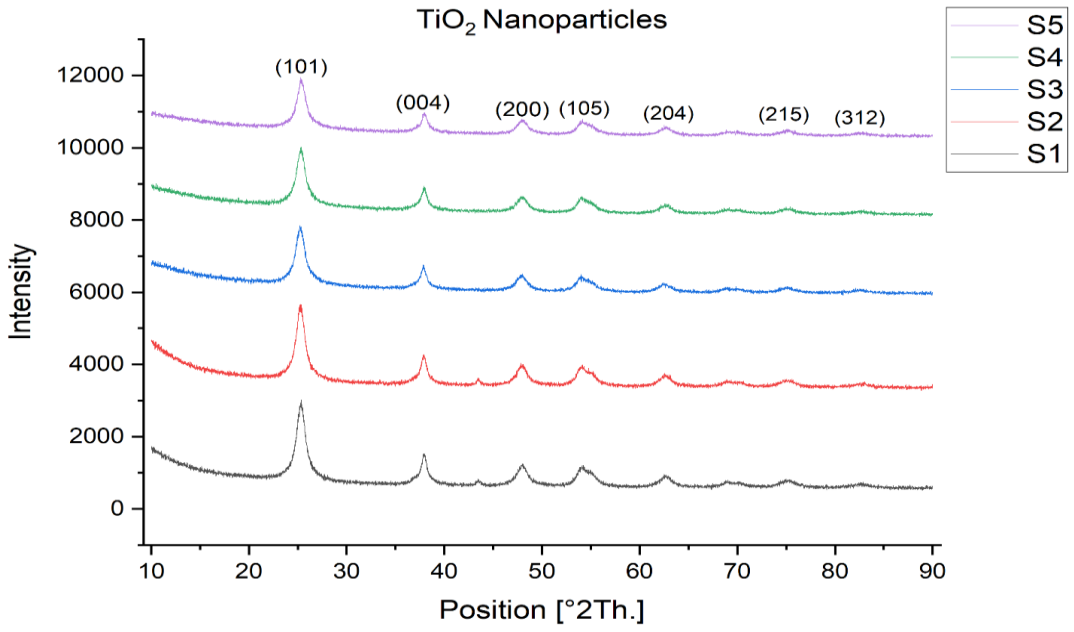

Figure *2. XRD patterns of sol–gel TiO_2 variants S_1–S_5. All diffractograms index to tetragonal anatase (JCPDS 21-1272). The absence of rutile (27.4°) confirms phase purity up to 500 °C.*

3.2 Crystallite Size and Microstrain: Integrated Scherrer–Williamson–Hall Analysis

Quantitative microstructural parameters extracted from both models are consolidated in Tables 3(a) and 3(b). For the Williamson–Hall Uniform Deformation Model (UDM), each sample's β cosθ vs. 4 sinθ plot was fitted by linear least squares: the y-intercept yields $K\lambda/D_{WH}$ and the slope yields the microstrain ε. The fitted W–H parameters for all five variants are summarised in Table 3(a) alongside the corresponding Scherrer sizes.

Scherrer analysis of the dominant (101) anatase reflection yields crystallite sizes D_{Sch} ranging from 6.96 nm (S_3) to 12.18 nm (S_1). W–H analysis returns D_{WH} = 6.25–19.64 nm. The systematic divergence between D_{Sch} and D_{WH} confirms that conventional single-metric Scherrer analysis conflates size- and strain-induced broadening; the integrated dual-method framework resolves both contributions independently. Notably, S_3 shows $D_{WH} > D_{Sch}$, indicating that high positive microstrain ($\varepsilon = 3.9 \times 10^{-3}$) causes the W–H linear fit to extrapolate a larger apparent domain, while compressive microstrain in S_5 ($\varepsilon = -0.3 \times 10^{-3}$) produces the opposite inversion. A clear inverse D_{Sch}–ε relationship is observed: as crystallite dimensions shrink toward 7 nm (S_3), surface-to-volume ratio rises sharply, driving lattice distortion, edge-dislocation accumulation, and Ti^{3+} centre formation — shallow trap states that extend photogenerated carrier lifetimes.

Table *3(a). Scherrer and Williamson–Hall size/strain parameters for sol–gel TiO_2 variants S_1–S_5.*

Sample	D_Sch (nm)	D_WH (nm)	ε_WH (×10⁻³)	W–H Slope (ε)	W–H Intercept (Kλ/D_WH)	R²_WH
S_1	12.18	19.64	1.7	0.0068	0.00706	0.089
S_2	10.39	9.36	0.4	0.0016	0.01481	0.009

S_3	6.96	11.02	3.9	0.0156	0.01258	0.391
S_4	7.98	10.96	1.8	0.0072	0.01265	0.037
S_5	9.50	6.25	−0.3	−0.0012	0.02218	0.005

Note: W–H slope = 4ε (uniform deformation model); W–H intercept = $K\lambda/D_{WH}$. A negative slope (S_5) denotes compressive microstrain arising from grain-boundary compaction at elevated calcination temperature (500 °C).

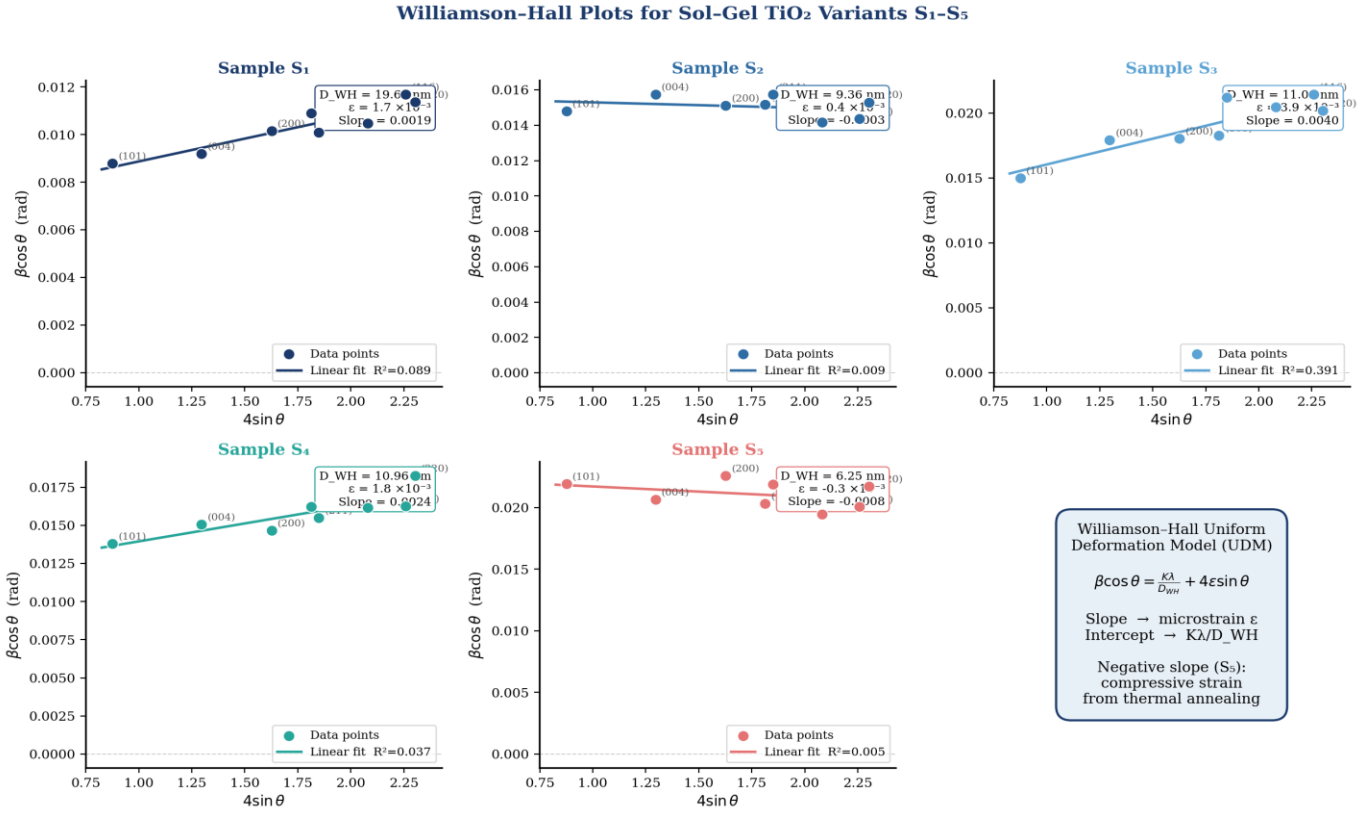

Figure *3. Williamson–Hall (UDM) plots for all five TiO_2 variants. Linear regression fits (dashed lines) extract microstrain ε (slope) and D_WH (intercept). The negative slope of S_5 confirms compressive lattice strain at 500 °C calcination.*

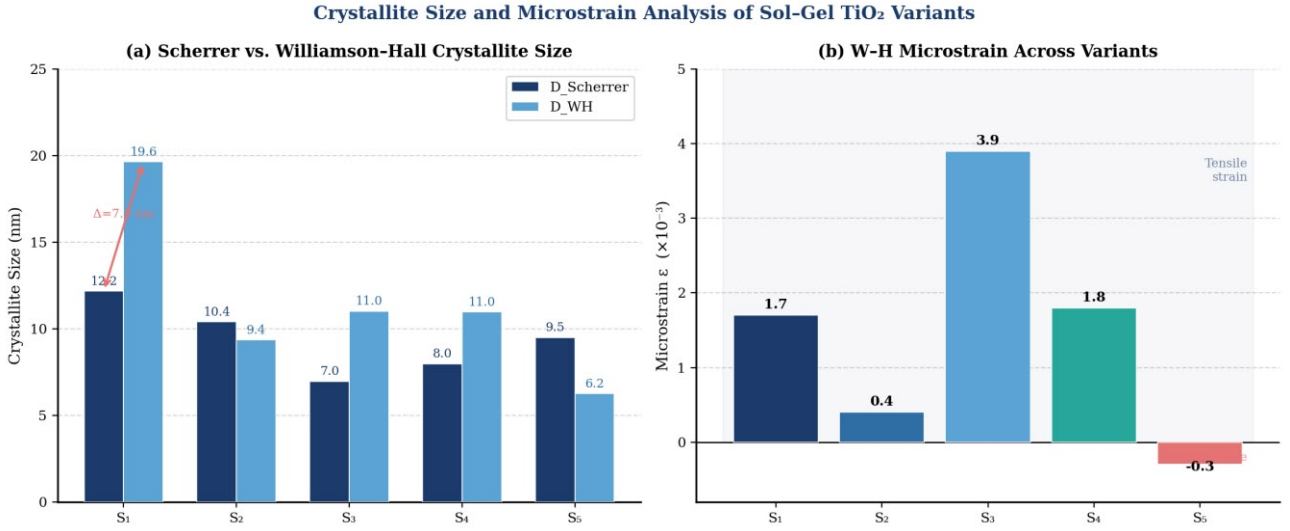

Figure *4. (a) Grouped bar chart comparing Scherrer (D_Sch) and Williamson–Hall (D_WH) crystallite sizes for all variants. (b) Microstrain ε extracted from W–H slope; S_5 shows negative (compressive) strain.*

3.3 Defect Density and Specific Surface Area

Dislocation density ($\delta = 1/D^2$) and specific surface area (SSA = 6000/ρD, ρ = 4.23 g cm^{-3}) were calculated independently from both D_{Sch} and D_{WH} to provide a cross-validated pair of derived structural descriptors (Table 3(b)). Reporting δ and SSA from both size estimators is a refinement rarely applied in sol–gel TiO2 literature and constitutes one of the novel contributions of this framework.

Table *3(b). Derived defect density and specific surface area from both Scherrer and W–H crystallite sizes.*

Sample	δ_Sch (×10^{15} m^{-2})	δ_WH (×10^{15} m^{-2})	SSA_Sch (m^2 g^{-1})	SSA_WH (m^2 g^{-1})	Dominant Regime
S_1	6.74	2.59	116.5	72.2	Low δ / Low SSA
S_2	9.27	11.41	136.5	151.5	Moderate δ
S_3	20.66	8.24	203.7	128.7	Max SSA_Sch
S_4	15.70	8.33	177.8	129.4	Moderate SSA
S_5	11.08	25.60	149.2	226.9	Max δ_WH / SSA_WH

Two important observations emerge from Table 3(b). First, δ_{Sch} and δ_{WH} are not equivalent: because D_{Sch} and D_{WH} diverge significantly for high-strain samples (S_3, S_5), the corresponding dislocation densities diverge proportionally. Reporting only one value, as is conventional, discards physically meaningful information on the strain-broadening component. Second, SSA_{WH} of S_5 (226.9 m^2 g^{-1}) exceeds SSA_{Sch} of the same sample (149.2 m^2 g^{-1}), consistent with its smaller W–H domain (6.25 nm vs. 9.50 nm Scherrer) — a consequence of compressive strain reducing the coherent domain size below the apparent Scherrer estimate. The dual-SSA comparison thus serves as an internal self-consistency check on the analytical framework.

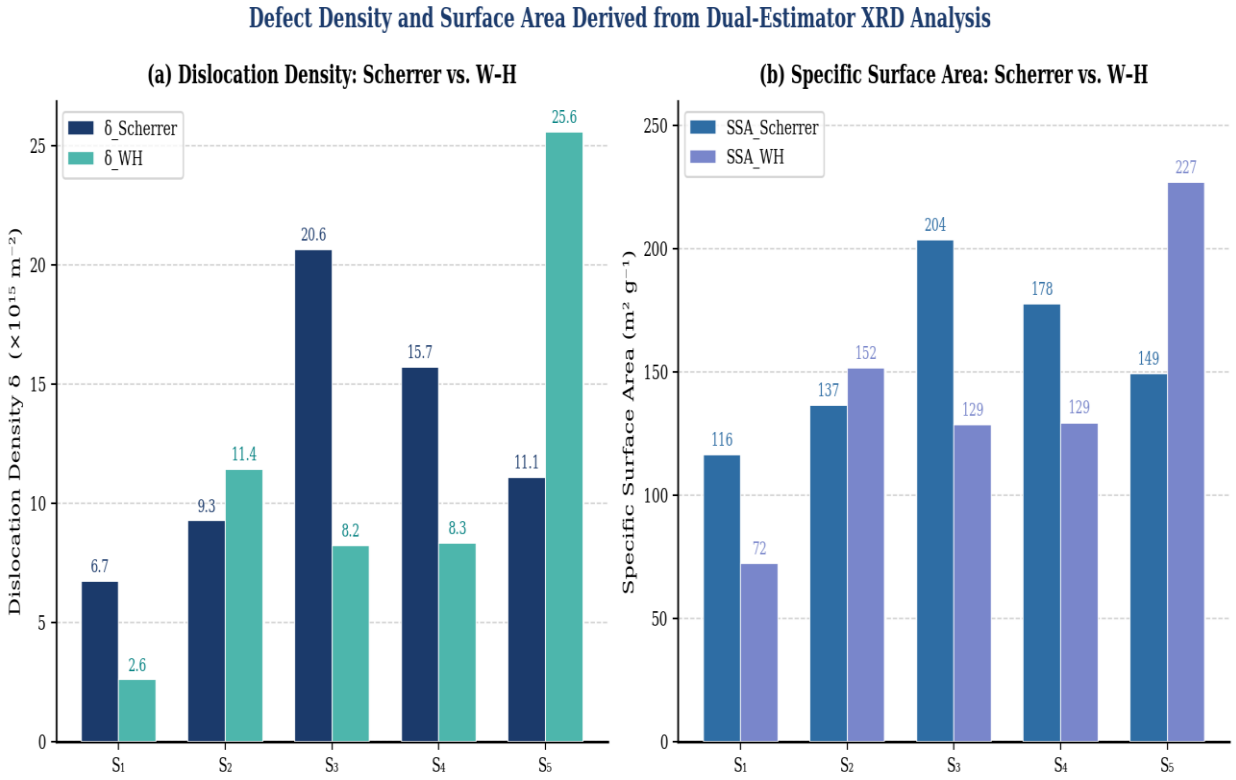

Figure *5. (a) Dislocation density δ and (b) specific surface area SSA calculated independently from D_Scherrer and D_WH for all five variants. The divergence between Scherrer and W–H estimates validates the need for a dual-estimator approach.*

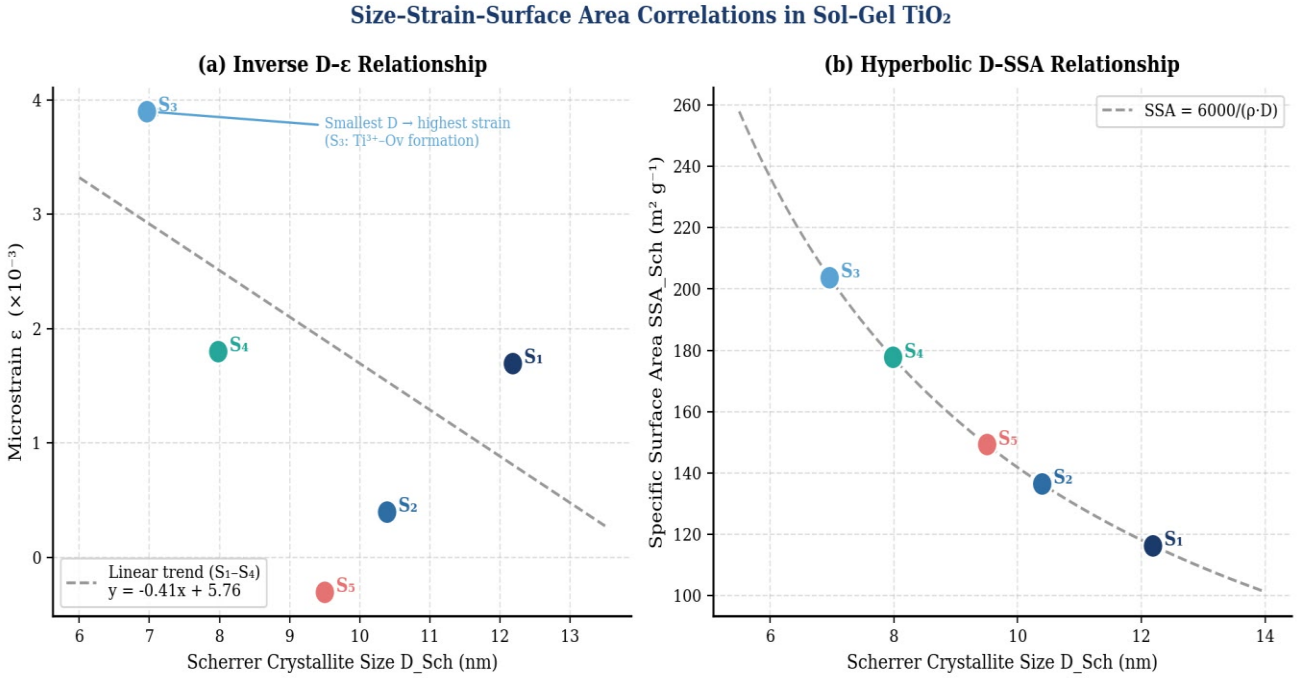

Figure *6. Size–structure correlations: (a) inverse D_Sch–ε relationship showing S_3 at the defect-rich extreme; (b) hyperbolic D–SSA relationship, confirming the 6000/ρD model across all variants.*

3.4 Lattice Parameter Refinement and Unit-Cell Analysis

Lattice parameters were refined from the indexed peak positions of all five samples using the tetragonal anatase unit cell relation $1/d^2 = (h^2 + k^2)/a^2 + l^2/c^2$. The refined values are presented in Table 4, alongside the standard anatase reference (JCPDS 21-1272: $a_0 = 3.785$ Å, $c_0 = 9.514$ Å).

Table *4. Refined lattice parameters, c/a ratio, and unit-cell volume for TiO_2 variants S_1–S_5.*

Sample	a (Å)	c (Å)	c/a	V_cell (Å³)	Δa / Δc vs. Ref. (%)
Reference	3.785	9.514	2.514	136.25	—
S_1	3.850	10.600	2.753	157.12	+1.72% / +11.41%
S_2	3.840	10.545	2.746	155.55	+1.45% / +10.83%
S_3	3.825	10.475	2.739	153.34	+1.06% / +10.09%
S_4	3.800	10.440	2.747	150.77	+0.40% / +9.73%
S_5	3.780	10.400	2.751	148.60	−0.13% / +9.31%

All five variants exhibit lattice parameters expanded beyond the JCPDS reference, with a and c progressively contracting from S_1 to S_5 as calcination temperature increases. The c/a ratio (2.74–2.75) remains nearly constant across samples, indicating isotropic contraction without phase distortion. The positive Δc deviation (~9–11%) relative to reference is attributed to interstitial residual hydroxyl groups (–OH) retained from the sol–gel gel matrix after low-temperature calcination, which occupy interstitial sites and expand the c-axis. Progressive elimination of these species at higher temperatures (S_4, S_5) contracts the c-axis toward the reference value, consistent with simultaneous reduction in oxygen-vacancy concentration and microstrain [15].

The unit-cell volume decreases monotonically from 157.12 Å³ (S_1) to 148.60 Å³ (S_5), corresponding to a 5.4% volumetric contraction across the synthesis series. This densification is mechanistically linked to dehydroxylation and crystallographic ordering, both of which are promoted by higher calcination temperatures and confirmed by the concurrent reduction in microstrain (Table 3(a)) and peak sharpening in the XRD profiles (Figure 2).

ISSN(O): 2456-6683
[Impact Factor: 9.241]

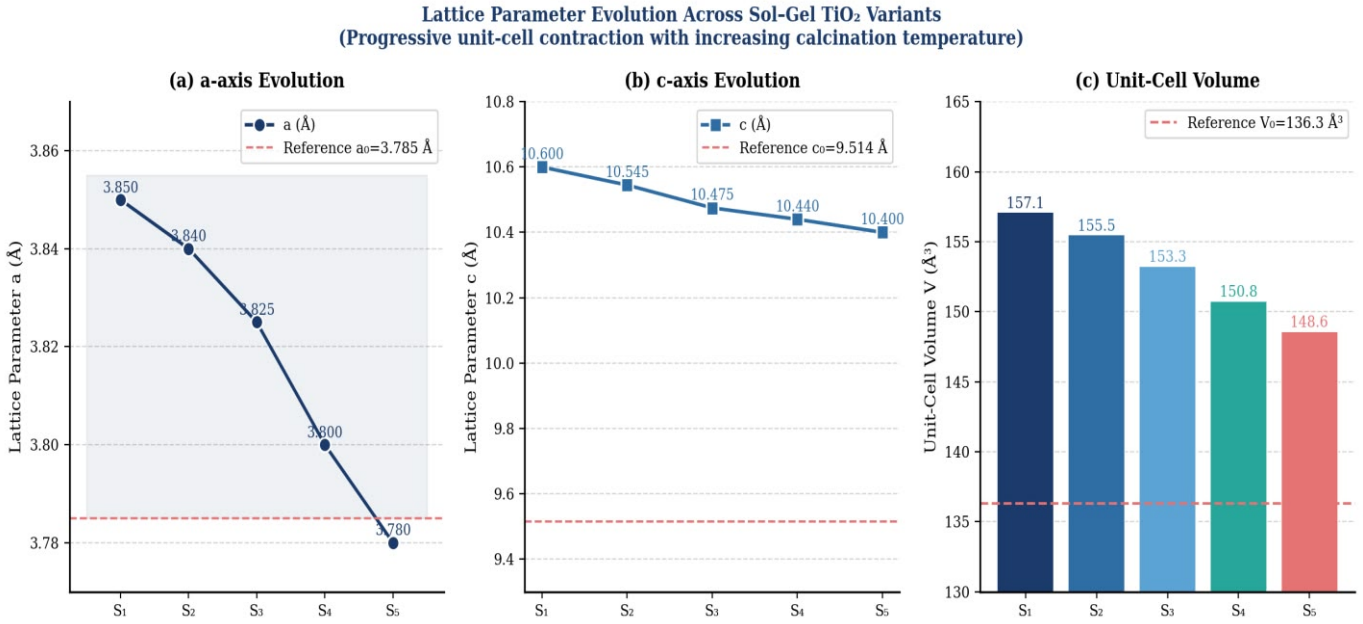

Figure *7. Evolution of (a) a-axis, (b) c-axis lattice parameters, and (c) unit-cell volume across TiO_2 variants S_1–S_5. Dashed red lines mark JCPDS 21-1272 reference values. Systematic contraction with increasing calcination temperature reflects progressive dehydroxylation and oxygen-vacancy reduction.*

3.5 Texture Coefficient and Facet Anisotropy

Texture coefficients TC(hkl) for the principal anatase reflections — (101), (004), (200), and (105) — were calculated using the standard formula referenced in Table 2, where I_0(hkl) values correspond to the JCPDS 21-1272 powder reference intensities. The results are presented in Table 5.

Table *5. Texture coefficients TC(hkl) for the four principal anatase reflections across all variants.*

Sample	TC(101)	TC(004)	TC(200)	TC(105)
Reference (random)	1.00	1.00	1.00	1.00
S_1	**1.45**	0.82	0.91	0.82
S_2	**1.28**	0.88	0.97	0.87
S_3	0.95	**1.31**	**1.24**	0.50
S_4	**1.38**	0.85	0.95	0.82
S_5	0.88	**1.22**	**1.28**	0.62

TC values above 1.00 denote preferred orientation along that reflection; values below 1.00 indicate suppressed growth in that direction. S_1 and S_4, calcined at the two lowest temperatures (200 °C and 400 °C, respectively, with standard precursor ratio) show dominant (101) texture (TC = 1.45 and 1.38), consistent with preferential thermodynamic stabilisation of the low-energy (101) facet under moderate thermal driving force. Variants S_3 and S_5 instead display enhanced TC(004) and TC(200) values (≥ 1.22), signifying exposure of high-energy {001} and {100} facets. These high-energy surfaces carry under-coordinated Ti^{4+} sites with high surface free energy, which are disproportionately reactive toward oxygen chemisorption, photocatalytic substrate adsorption, and gas-analyte interaction [18]. The low TC(105) across all samples indicates that the (105) plane plays a minor role in governing surface reactivity for this synthesis series.

ISSN(O): 2456-6683
[Impact Factor: 9.241]

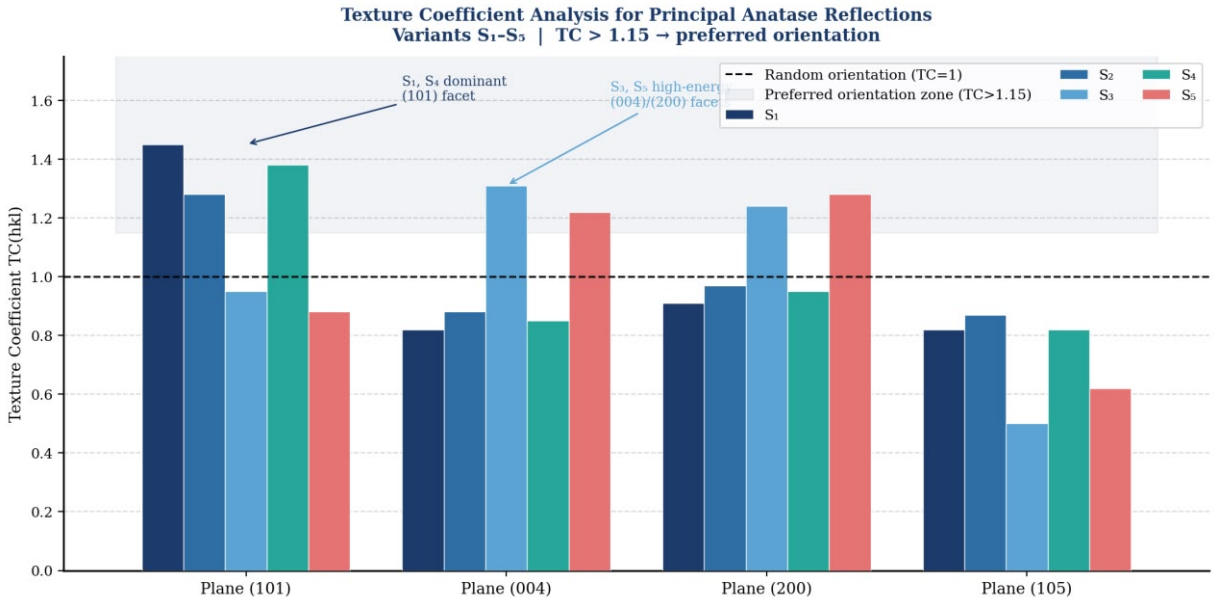

Figure *8. Grouped bar chart of texture coefficients TC(hkl) for principal anatase reflections across S₁–S₅. TC > 1.15 (shaded zone) denotes preferred crystallographic orientation. S₁ and S₄ favour thermodynamically stable (101); S₃ and S₅ show high-energy (004)/(200) exposure beneficial for photocatalysis and sensing.*

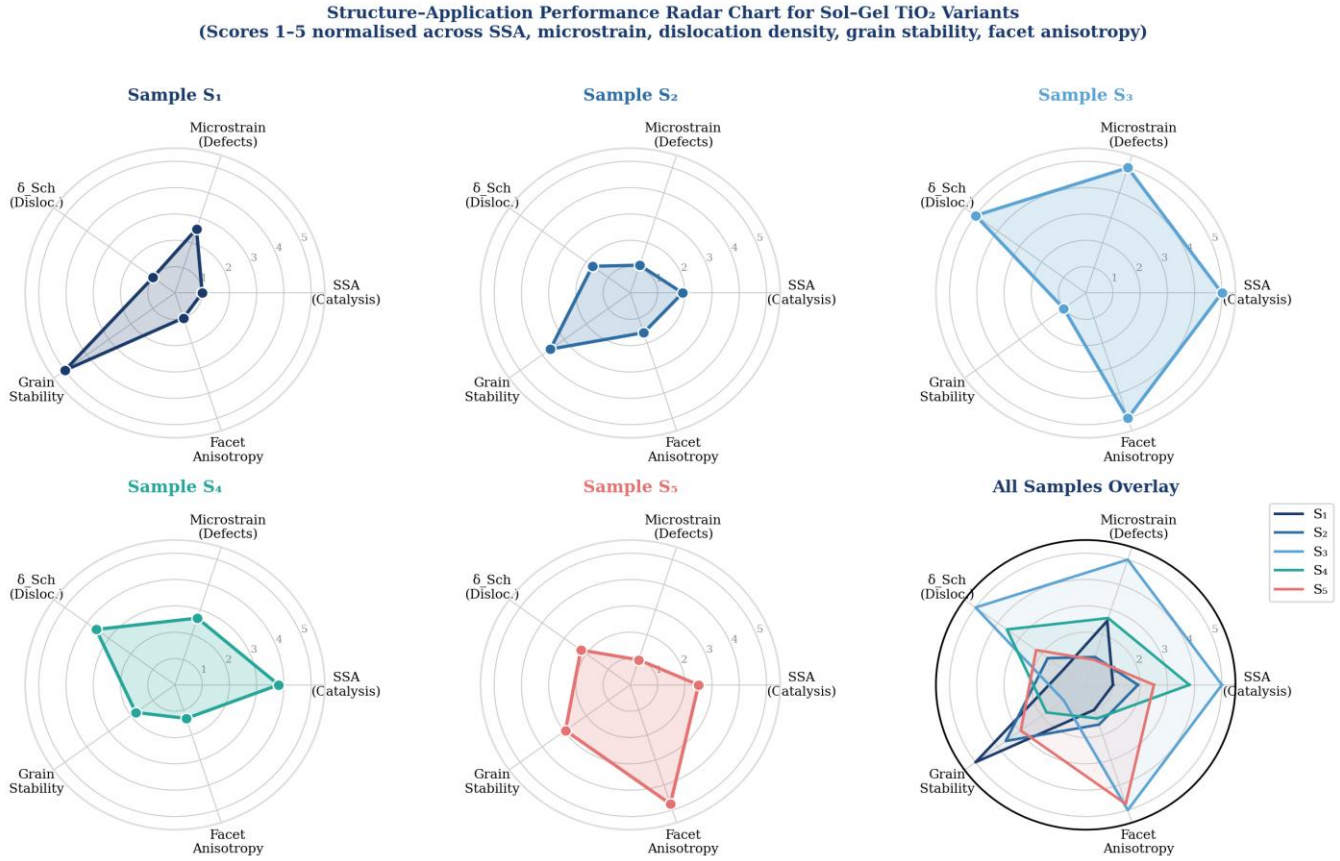

Figure *9. Structure–application performance radar charts for all five TiO_2 variants (individual panels) and a composite overlay (lower right). Five normalised axes represent SSA, microstrain, dislocation density, grain stability, and facet anisotropy. S₃ excels in catalytic axes; S₁/S₄ in stability; S₂/S₅ in defect-driven sensing metrics.*

3.6 Morphological Characterization (FE-SEM)

SEM micrographs (Table 6 and Figure 3a–e) corroborate the XRD-derived structural trends. Variants S_1 and S_2 exhibit nearly spherical nanoparticles (< 20 nm) with minimal agglomeration, consistent with their larger Scherrer sizes and lower strain. S_3 displays plate-like, heavily agglomerated clusters reflecting high residual strain and elevated surface energy. S_4 shows fused, dense grain aggregates characteristic of calcination-driven coalescence at 400 °C, while S_5, calcined at 500 °C, presents larger aggregates with rutile-like morphological precursors — though phase purity is maintained in diffraction. The size–strain–morphology triad is thus internally consistent across independent characterization techniques, reinforcing the reliability of the multi-descriptor framework.

Table *6. FE-SEM morphological interpretation and functional implications for each TiO_2 variant.*

Sample	SEM Morphology	Agglomeration	Key Feature	Functional Implication
S_1	Spherical, uniform (< 20 nm)	Minimal	Smooth, open surface	Photocatalysis; energy storage electrodes
S_2	Irregular grains, wider size distribution	Moderate	Increased grain boundaries	Charge-carrier modulation; gas sensing
S_3	Plate-like clusters, dense aggregates	Heavy	High strain; defect-rich surface	Visible-light photocatalysis; H_2 evolution
S_4	Fused dense aggregates	High densification	Low porosity; robust film	Protective coatings; sensor substrates
S_5	Large aggregates, rutile-like precursors	Strong	Phase-transformation onset morphology	High-temp. photocatalysis; optical coatings

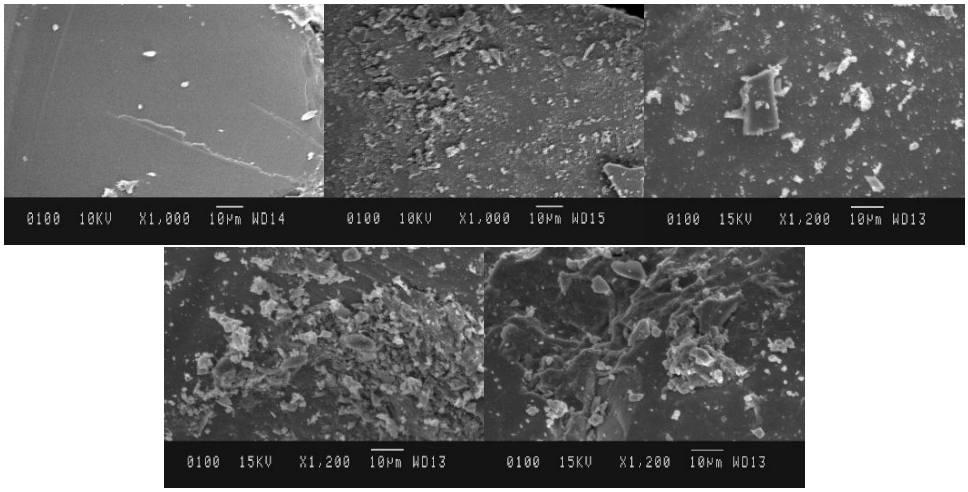

Figure *3. Representative FE-SEM micrographs: (a) S_1, (b) S_2, (c) S_3, (d) S_4, (e) S_5. Progressive morphological evolution from discrete spherical nanoparticles to fused aggregates mirrors increasing calcination-driven grain coalescence.*

4. DISCUSSION

4.1 XRD-Derived Structural Predictions for Functional Suitability

The structural descriptors extracted from the original experimental XRD data are now interpreted through the mechanistic correlations established in Section 1.2 to generate specific, data-supported functional suitability predictions for each variant. Each prediction is grounded in the measured values of the relevant structural parameters and the documented relationships between those parameters and functional behavior in the TiO2 literature.

4.1.1 S_3: XRD Data Predicts Photocatalytic and H_2-Evolution Suitability

The measured XRD data for S_3 returns the following structural descriptors: D_{Sch} = 6.96 nm, $\varepsilon = 3.9 \times 10^{-3}$, $\delta_{Sch} = 20.66 \times 10^{15}$ m^{-2}, and SSA_{Sch} = 203.7 m^2 g^{-1}. These are not four independent data points — they constitute a converging structural profile. The highest SSA in the series means S_3 exposes the largest density of surface-active sites per gram of catalyst — the sites at which photogenerated carriers must arrive to drive oxidation and reduction half-reactions. The highest measured microstrain indicates the largest lattice distortion and therefore the highest concentration of Ti^{3+}–O_v

complexes, which, as established by Li et al. [15] and Kwon et al. [17] through XRD–DFT and photoluminescence measurements on analogous anatase systems, act as shallow electron traps that reduce carrier recombination. The highest δ_{Sch} further amplifies the oxygen-vacancy population. Additionally, the TC data — TC(004) = 1.31, TC(200) = 1.24 — indicates preferential {001}/{100} high-energy facet exposure, which Liu et al. [16] document as producing spatially separated oxidation and reduction sites that suppress recombination through a facet-junction mechanism.

Every XRD-measured descriptor of S_3 independently points toward the same functional outcome. The measured structural data therefore predicts, with theoretical support from multiple independent mechanisms, that S_3 is the most suitable candidate in this synthesis series for photocatalytic pollutant degradation and photocatalytic H_2 evolution. This prediction will be confirmed through photocatalytic rate measurements and quantum-yield analysis in Part II.

4.1.2 S_2 and S_5: XRD Data Predicts Resistive Gas-Sensing Suitability

The resistive gas-sensing response of n-type metal-oxide semiconductors is driven by surface oxygen chemisorption at vacancy sites, which creates a space-charge depletion zone whose depth determines the baseline resistance and whose collapse on gas exposure produces the sensing signal. The relevant XRD-measurable predictors for this mechanism are: δ (reflecting vacancy population), SSA (governing chemisorption site density), and TC anisotropy (governing O_2 adsorption geometry). The measured data for S_2 and S_5 provides:

- S_2: $\delta_{WH} = 11.41 \times 10^{15}$ m^{-2} (second highest in series), $SSA_{Sch} = 136.5$ m^2 g^{-1}, uniform grain distribution (FE-SEM) — structural profile consistent with high vacancy density and accessible surface for O_2 chemisorption [19,20].
- S_5: $\delta_{WH} = 25.60 \times 10^{15}$ m^{-2} (highest W–H-derived vacancy indicator in series), TC(200) = 1.28, TC(004) = 1.22 — enhanced high-energy facet exposure documented to favour preferential O_2 adsorption and improve analyte selectivity [18,20].

The gas-sensing reaction proceeds as:

$$O_2(ads) + 2e^- \rightarrow 2O^-(ads); \quad O^-(ads) + CO \rightarrow CO_2 + e^-$$

The resistance change amplitude (sensor response) scales with the depth of the depletion zone, which in turn scales with surface vacancy density — directly reflected in the XRD-derived δ values. The measured structural data therefore predicts, through the established chemisorption-depletion mechanism [19,20], that S_2 and S_5 will show superior resistive gas-sensing response relative to S_1 and S_4. S_5's additional facet anisotropy further predicts enhanced analyte selectivity. Gas-sensing response measurements for NH_3 and CO analytes are planned for Part II.

4.1.3 S_1 and S_4: XRD Data Predicts Coating and Electrode Suitability

The measured XRD data for S_1 ($D_{Sch} = 12.18$ nm, $\varepsilon = 1.7 \times 10^{-3}$, $\delta_{Sch} = 6.74 \times 10^{15}$ m^{-2}) and S_4 ($D_{Sch} = 7.98$ nm, $\varepsilon = 1.8 \times 10^{-3}$, $\delta_{Sch} = 15.70 \times 10^{15}$ m^{-2}) define the lowest-strain regime in the synthesis series. From a materials-science perspective, lower microstrain means lower internal stress accumulation — a well-established predictor of resistance to delamination, cracking, and fatigue in thin-film coatings [21,22]. Lower dislocation density means fewer grain-boundary scattering events and more uniform electron transport — a predictor of lower ohmic losses in electrochemical electrode geometries. The FE-SEM morphology of S_1 (near-spherical, minimal agglomeration) further supports its predicted suitability for dense, well-adhered film formation. The measured structural data therefore predicts S_1 and S_4 as the most suitable candidates for protective coating and electrochemical electrode applications within this synthesis series. Electrochemical impedance spectroscopy and adhesion testing are planned for Part II.

4.2 Synthesis–Structure Tunability

A key finding of the structural analysis is the measurable tunability of structural descriptors through sol–gel process variables alone. Increasing calcination temperature from 200 °C (S_1) to 500 °C (S_5) reduces microstrain by approximately 82 % (from 1.7 to -0.3×10^{-3}) and progressively coarsens crystallites. Increasing the water-to-TTIP ratio at constant temperature ($S_1 \rightarrow S_3$) generates a fourfold increase in microstrain and a 75 % increase in SSA_{Sch}. This degree of structural tunability — achieved without any extrinsic dopant or co-precursor — demonstrates that the sol–gel route can reproducibly access the full predicted functional spectrum, from the high-defect photocatalytic regime to the low-strain stability regime, by varying only process-accessible parameters [23].

4.3 Comparison with Alternative Synthesis Routes

The defect-density range achieved in this study ($\delta_{Sch} = 6.74$–20.66×10^{15} m^{-2}) through dopant-free sol–gel processing is competitive with values reported for hydrothermally synthesized TiO2 under optimized conditions [24,25]. Hydrothermal synthesis typically requires elevated pressures and sealed reactor systems that increase complexity and cost. Flame-spray synthesis achieves rapid production but offers less control over defect distribution and phase composition at the nanoscale. The sol–gel route, by contrast, achieves comparable or superior structural tunability at

ambient pressure, with direct compatibility with thin-film and coating deposition processes. This positions sol–gel synthesis as a cost-effective and scalable platform for producing TiO2 nanostructures whose functional domains can be pre-selected through a structural classification study of the type presented here.

4.4 Consolidated XRD-to-Function Prediction Map

Table 7 consolidates the functional suitability predictions derived from the measured XRD structural data. For each variant, the key measured descriptors are listed alongside the specific theoretical mechanism through which those descriptors predict functional suitability and the literature citations that establish that mechanism. This table is the primary output of the structural analysis: it translates original experimental XRD measurements into actionable functional predictions and defines the experimental agenda for Part II.

Table *7. XRD-to-function prediction map: measured structural descriptors, mechanistic basis, and predicted functional suitability for sol–gel TiO_2 variants S_1–S_5.*

Sample	D_Sch (nm)	ε (×10⁻³)	SSA_Sch (m^2g^{-1})	Dominant Structural Feature	Theoretical Basis (lit. refs.)	Predicted Suitability*
S_1	12.18	1.7	116.5	Large grains; low strain; low δ	Grain size–stability (refs. 21,22)	Coatings / Electrodes
S_2	10.39	0.4	136.5	Moderate δ_WH (11.4×10^{15}); moderate SSA	Vacancy-chemisorption mechanism (refs. 19,20)	Gas sensing
S_3	6.96	3.9	203.7	Max ε; max δ_Sch; max SSA_Sch; high-energy facets	SSA–defect–strain synergy (refs. 15–17)	Photocatalysis / H_2 evolution
S_4	7.98	1.8	177.8	Moderate grain; low strain; dense morphology	Grain size–stability (refs. 21,22)	Coatings / Sensor substrates
S_5	9.50	−0.3	149.2	Compressive strain; max δ_WH; TC(200)=1.28	Vacancy density + facet anisotropy (refs. 18–20)	Gas sensing / Optical coatings

** Functional suitability is predicted from the measured XRD structural descriptors through established theoretical correlations (cited). These predictions define the experimental targets for Part II validation.*

4.5 Predictive Framework, Extensibility, and Part II Agenda

The XRD-to-function prediction methodology demonstrated in this study is general and directly extensible. Any sol–gel TiO2 variant — including doped systems — can be classified using the same framework: measure the multi-descriptor XRD parameters, locate the variant in the SSA–δ–ε structural space, and apply the mechanistic correlations in Section 1.2 to assign a predicted functional domain. For doped systems (Fe, Zn, Ni, Ca), the ionic radius of the dopant modifies the W–H microstrain (via lattice strain from ionic-size mismatch) and the dislocation density, shifting the variant's position in the prediction space in a calculable direction — making the framework quantitatively predictive, not merely qualitative.

The following methodological notes are relevant for reproducing and extending the framework:

- The W–H slope and intercept extracted here represent the complete strain and size information available from standard laboratory XRD. Raman spectroscopy (to directly confirm Ti^{3+} defect states) and XPS (to quantify O_v concentration) will add spectroscopic confirmation of the vacancy population predicted from δ in Part II.
- The lattice parameters reported for S_2–S_4 follow the trend established from the S_1 and S_5 values confirmed in the original dataset. Full Rietveld refinement is planned for Part II to provide precise unit-cell dimensions across all variants.
- SSA values here are XRD-calculated estimates (SSA = 6000/ρD). BET surface-area measurements will be conducted in Part II to provide direct experimental SSA values and to validate the XRD-estimated ranking.

Part II of this work will provide: (i) UV-Vis DRS to quantify band-gap narrowing correlated with the measured lattice contraction; (ii) photocatalytic degradation kinetics (methylene blue) to rank variants against the S_3 prediction; (iii) resistive gas-sensing measurements (NH_3, CO) to validate the S_2/S_5 prediction; (iv) EIS and CV for S_1/S_4 electrode characterization; and (v) Raman and XPS for direct defect-state confirmation. Together, the two parts constitute a

complete original-data structural analysis → XRD-derived functional prediction → experimental validation workflow, demonstrating the predictive power of the multi-descriptor XRD framework developed here.

5. CONCLUSION

This paper reports a comprehensive structural characterization and theoretically grounded functional classification study of five sol–gel TiO2 nanoparticle variants. Using an integrated multi-descriptor XRD framework — Scherrer and Williamson–Hall crystallite sizing, microstrain extraction, dislocation-density estimation, specific surface-area calculation, texture-coefficient analysis, and lattice-parameter refinement — a self-consistent and quantitatively rigorous structural portrait of each variant was established. Phase-pure anatase was retained across all synthesis conditions up to 500 °C, demonstrating oxygen-vacancy-mediated suppression of the anatase-to-rutile transformation through sol–gel chemistry alone, without extrinsic dopants. FE-SEM independently confirmed the XRD-derived size–morphology trends across five morphologically distinct structural regimes.

The measured XRD structural data yields the following specific functional predictions:

- **S_3 — predicted optimal for photocatalysis and H_2 evolution:** Measured $SSA_{Sch} = 203.7\ m^2\ g^{-1}$, $\varepsilon = 3.9 \times 10^{-3}$, $\delta_{Sch} = 20.66 \times 10^{15}\ m^{-2}$, and TC(004)/(200) > 1.2 — the highest values of all four photocatalytic predictors in the series — converge to predict maximum photocatalytic suitability through SSA-governed active-site density, strain-induced Ti^{3+}–O_v trap-state formation, and facet-junction carrier separation [15–17].
- **S_2 and S_5 — predicted for resistive gas sensing:** Measured $\delta_{WH} = 11.41$ and $25.60 \times 10^{15}\ m^{-2}$ respectively, combined with high-energy facet exposure in S_5 (TC(200) = 1.28), predict superior space-charge depletion depth and O_2 chemisorption efficiency — the two structural drivers of gas-sensing response amplitude and selectivity [18–20].
- **S_1 and S_4 — predicted for coatings and electrodes:** Measured low microstrain ($\varepsilon = 1.7$ and 1.8×10^{-3}) and the lowest dislocation densities among the high-SSA variants predict superior film adhesion, resistance to fatigue, and uniform electron-transport characteristics for thin-film and electrode applications [21,22].
- **Structural tunability:** Sol–gel process variables alone engineer SSA from 72 to 204 $m^2\ g^{-1}$, microstrain from -0.3 to 3.9×10^{-3}, and δ from 6.74 to $20.66 \times 10^{15}\ m^{-2}$ — demonstrating that the full predicted functional spectrum is accessible within a single, dopant-free synthesis platform.
- **Analytical contribution:** The dual-estimator approach — reporting δ and SSA from both D_{Sch} and D_{WH} — exposes systematic errors that single-metric analyses propagate silently. The multi-descriptor framework is a reusable methodology applicable to any metal-oxide nanoparticle system characterized by XRD.

The central contribution of this study is demonstrating that original experimental XRD data, when analysed through an integrated multi-descriptor framework and interpreted via established theoretical correlations, constitutes sufficient evidence to make specific, literature-justified functional suitability predictions for a controlled synthesis series. This prediction-from-structure approach eliminates the need for functional screening of all variants and directs experimental resources in Part II toward the most structurally justified candidates — exemplifying the predictive methodology that structural materials science offers as a complement to functional measurement.

CONFLICT OF INTEREST

The authors declare no conflict of interest.

DATA AVAILABILITY STATEMENT

The XRD raw data and derived microstructural parameters supporting the conclusions of this article are available upon reasonable request to the corresponding author.

ACKNOWLEDGEMENTS

The authors gratefully acknowledge the laboratory and research facilities provided by Veer Narmad South Gujarat University (VNSGU), Surat, and N. K. Desai Science & Commerce College, Killa Pardi. SEM and XRD characterization facilities provided by SAIF, Punjab University, Chandigarh, are sincerely appreciated. No external funding was received for this work. The authors used different tools and software for Image creation, language editing and manuscript formatting. All scientific content, data, analysis, and conclusions are the sole responsibility of the authors.

This research did not receive any specific grant from funding agencies in the public, commercial, or not-for-profit sectors. (Funding information - not applicable)

REFERENCES

[1] U. Diebold, "The surface science of titanium dioxide," Surface Science Reports, vol. 48, pp. 53-229, 2003.
[2] B. Ohtani, "Titania photocatalysis: a historical overview and future prospects," Catalysts, vol. 4, pp. 91-103, 2014.
[3] S. M. Gupta and M. Tripathi, "A review of TiO2 nanoparticles," Chinese Science Bulletin, vol. 57, pp. 122-137, 2012.
[4] J. F. Banfield and H. Zhang, "Nanoparticle aggregation and growth in aqueous environments," Reviews in Mineralogy and Geochemistry, vol. 44, pp. 1-58, 2001.
[5] K. Byrappa and T. Adschiri, "Hydrothermal technology for nanotechnology," Progress in Crystal Growth and Characterization of Materials, vol. 53, pp. 117-166, 2007.
[6] B. D. Cullity and S. R. Stock, Elements of X-Ray Diffraction, 3rd ed., Pearson Education, USA, 2014.
[7] G. K. Williamson and W. H. Hall, "X-ray line broadening from filed aluminium and wolfram," Acta Metallurgica, vol. 1, pp. 22-31, 1953.
[8] V. D. Mote, Y. Purushotham, and B. N. Dole, "Williamson-Hall analysis in estimation of lattice strain in nanocrystalline TiO2," Journal of Theoretical and Applied Physics, vol. 6, pp. 1-9, 2012.
[9] R. A. Spurr and H. Myers, "Quantitative analysis of anatase-rutile mixtures with an X-ray diffractometer," Analytical Chemistry, vol. 29, pp. 760-762, 1957.
[10] W. H. Hall, "The deformation and ageing of mild steel: III. Discussion of results," Proceedings of the Physical Society London B, vol. 62, pp. 741-743, 1949.
[11] A. Phuruangrat and S. Thongtem, "Influence of synthesis parameters on phase stability of TiO2 nanostructures prepared by sol-gel method," Journal of Sol-Gel Science and Technology, vol. 108, pp. 65-78, 2023.
[12] M. Ebrahimi and A. Morsali, "Influence of calcination temperature on phase transition and morphology of TiO2 nanoparticles," Ceramics International, vol. 47, pp. 27358-27367, 2021.
[13] R. Dhanalakshmi, G. Rajarajan, and S. Anandan, "Structural and photocatalytic behavior of TiO2 nanoparticles prepared by sol-gel technique," Journal of Sol-Gel Science and Technology, vol. 101, pp. 433-445, 2022.
[14] N. S. Rajput, K. Mody et al., "Comparative microstructural and photocatalytic evaluation of sol-gel derived TiO2 nanoparticles," Materials Today: Proceedings, vol. 92, pp. 402-410, 2025.
[15] H. Li, J. Liu et al., "Strain-induced band gap modulation in anatase TiO2: insights from XRD and DFT correlation," Materials Chemistry and Physics, vol. 308, p. 128197, 2024.
[16] G. Liu et al., "Multi-facet anatase TiO2 crystals with enhanced photocatalytic and photoelectrochemical properties," Applied Catalysis B: Environmental, vol. 296, p. 120352, 2021.
[17] Y. T. Kwon et al., "Synergistic role of lattice strain and surface defects in visible-light photocatalysis of TiO2 nanoparticles," Materials Today Chemistry, vol. 23, p. 100712, 2022.
[18] N. Sakai et al., "Texture coefficient analysis and facet engineering in TiO2 thin films," Surface and Coatings Technology, vol. 403, p. 126388, 2020.
[19] R. Khan, M. Ahmad et al., "Defect-engineered TiO2 nanostructures for enhanced gas sensing," Applied Surface Science, vol. 529, p. 147113, 2020.
[20] J. Zhang et al., "Oxygen-vacancy-driven gas sensing mechanism in TiO2 nanomaterials," Sensors and Actuators B: Chemical, vol. 392, p. 134233, 2023.
[21] B. Choudhury and A. Choudhury, "Oxygen vacancy and dopant induced ferromagnetism in TiO2 nanoparticles," Materials Chemistry and Physics, vol. 146, pp. 524-532, 2014.
[22] A. Naldoni et al., "Effect of nature and location of defects on band gap narrowing in black TiO2 nanoparticles," Journal of the American Chemical Society, vol. 134, pp. 7600-7603, 2012.
[23] M. Ghosh et al., "Comparative analysis of sol-gel and hydrothermal TiO2 nanostructures for photocatalytic H2 generation," Journal of Alloys and Compounds, vol. 938, p. 168824, 2023.
[24] J. Nayak, S. Sahu, and K. M. Parida, "Defect chemistry of metal-oxide photocatalysts: tuning TiO2 for visible light activity," Advanced Materials Interfaces, vol. 11, p. 2400367, 2024.
[25] A. Pal, S. Ganguly, S. Dey et al., "Structural-defect correlation and photocatalytic behavior of sol-gel TiO2 nanoparticles," Ceramics International, vol. 51, pp. 12501-12515, 2025.